J. Biophotonics **4**, No. 11–12, 824–839 (2011) / **DOI** 10.1002/jbio.201100049

Journal of BIOPHOTONICS

FULL ARTICLE

Comparison of permissible source region and multispectral data using efficient bioluminescence tomography method

Chenghu Qin[**,1], *Shouping Zhu*[**,2], *Jinchao Feng*[3], *Jianghong Zhong*[1], *Xibo Ma*[1], *Ping Wu*[1], *and Jie Tian*[*,1,2]

[1] Intelligent Medical Research Center, Institute of Automation, Chinese Academy of Sciences, Beijing 100190, China
[2] Life Sciences Research Center, School of Life Sciences and Technology, Xidian University, Xi'an, Shaanxi 710071, China
[3] College of Electronic Information & Control Engineering, Beijing University of Technology, Beijing 100124, China

Received 8 June 2011, revised 20 September 2011, accepted 20 September 2011
Published online 14 October 2011

Key words: Optical molecular imaging, bioluminescence tomography, permissible source region, spectrally resolved measurements, iterative shrinkage thresholding method

As a novel molecular imaging technology, bioluminescence tomography (BLT) has become an important tool for biomedical research in recent years, which can perform a quantitative reconstruction of an internal light source distribution with the scattered and transmitted bioluminescent signals measured on the external surface of a small animal. However, BLT is severely ill-posed because of complex photon propagation in the biological tissue and limited boundary measured data with noise. Therefore, sufficient *a priori* knowledge should be fused for the uniqueness and stability of BLT solution. Permissible source region strategy and spectrally resolved measurements are two kinds of *a priori* knowledge commonly used in BLT reconstruction. This paper compares their performance with simulation and *in vivo* heterogeneous mouse experiments. In order to improve the efficiency of large-scale source restoration, this paper introduces an efficient iterative shrinkage thresholding method that not only has faster convergence rate but also has better reconstruction accuracy than the modified Newton-type optimization approach. Finally, a discussion of these two kinds of *a priori* knowledge is given based on the comparison results.

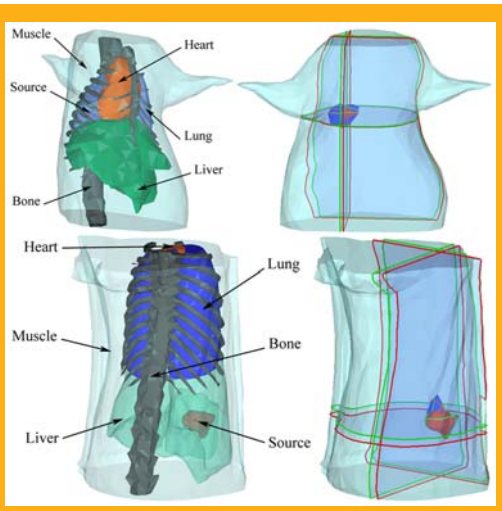

Mouse-shaped numerical and *in vivo* imaging experiments.

* Corresponding author: e-mail: tian@ieee.org, Phone: +86-10-82618465, Fax: +86-10-62527995
** Chenghu Qin and Shouping Zhu contributed equally to this work.

1. Introduction

Molecular imaging is a rapidly developing interdiscipline that involves molecular biology, mathematics, chemistry, physics, information science, medicine, pharmacology, etc. [1–3]. Molecular imaging technology can realize noninvasive *in vivo* imaging for biology organic physiological and pathological variation at the cellular and molecular levels, providing an effective method of information acquiring and analysis processing for life-science research [4–8]. Among molecular imaging techniques, optical imaging has attracted increasing attention in the biomedical field, and the modern molecular biology and the advanced optical imaging technologies are being combined to study biological and medical processes *in vivo* as well as diagnosing and managing diseases better [9–11]. As a promising optical molecular imaging modality, bioluminescence tomography (BLT) has become a research focus over the past few years in view of its high sensitivity, nonionization, high specificity, noninvasion, low background noise and high cost-effectiveness, which can be used for tumorigenesis study, cancer diagnosis, metastasis detection, drug discovery, gene therapy, etc. [12–16]. With the research of BLT, significant breakthroughs have been obtained in imaging theory, reconstruction algorithm and prototype instruments [17–30]. It should be emphasized that the biomedical applications of BLT have been greatly promoted by the progress of bioluminescent source restoration methods [11, 16, 31–33].

According to the uniqueness theory of inverse source reconstruction in the previous study, BLT is severely ill-posed for highly scattering property of the biological tissue and the limited surface measurements with noise [13]. Therefore, adequate *a priori* knowledge is essential for the uniqueness and stability of BLT solution [13, 15–17]. As we all know, the permissible source region and multispectral information are two commonly used strategies for reducing the ill-posedness of the inverse source recovery [15, 17, 20, 21, 24, 25, 34–41]. The permissible source region can be determined using the surface bioluminescent light spatial distribution and other prior information obtained from the specific biomedical application, such as anatomical structure and optical properties of the small animal [21, 36, 42]. The goal of this approach is to initially identify the possible region where the internal bioluminescent source locates from the whole biological tissue, and the number of unknowns to be solved is reduced largely, so the reconstruction can be improved [24, 27]. However, the permissible source region should be large enough to contain the actual source, and sometimes it can not be reliably chosen, especially for the deeper and/or multiple-source cases [16, 20, 36]. On the other hand, the application of multispectral information is regarded as another effective method to reduce the ill-posed nature of BLT [16, 27, 40]. Spectrally resolved measurements by a series of filters consider the wide emission spectra characteristic of bioluminescent reporters and the diversity of tissue optical properties for different spectral bands, which can increase the amount of known boundary data and reduce the ill-posedness of BLT [16, 27]. With the help of a focused ultrasound array, multispectral measurements have also been obtained because the source has a certain spectral red shift when the temperature of the luciferase enzymes is increased [43]. Furthermore, a more practical quasispectral method has been studied, and it should actually belong to spectrally resolved *a priori* information [40]. However, the corresponding computational efficiency will be greatly debased for the large-scale spectrally resolved source reconstruction. Therefore, the study of fast inversion algorithms is becoming ever more important with the size increase of detectable data sets in the spectrally resolved method [11]. The schematic diagram of the above two kinds of *a priori* knowledge commonly used in BLT is shown in Figure 1. From Figure 1, we can see that the permissible source region strategy can decrease the size of variables to be solved, and the spectrally resolved method can increase the amount of known data. This manuscript compares the permissible source region strategy and spectrally resolved measurements for

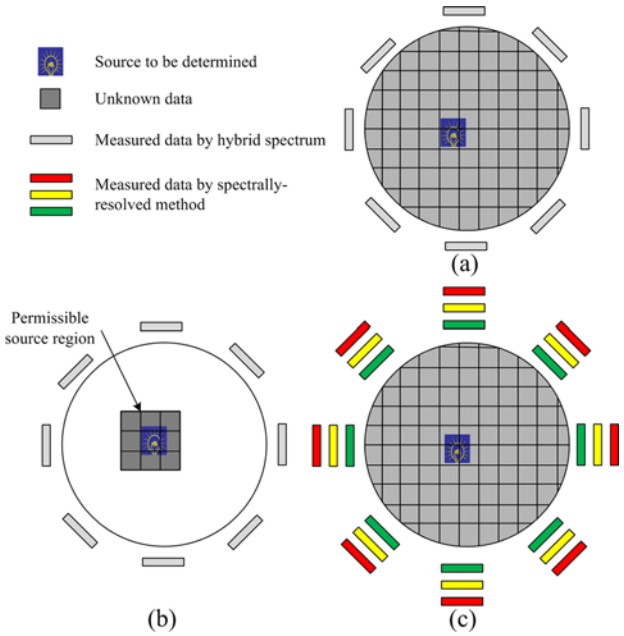

Figure 1 (online color at: www.biophotonics-journal.org) Diagrammatic sketch of strategies for reducing the ill-posedness of the inverse source recovery: (**a**) is the inverse source problem without any *a priori* knowledge; (**b**) and (**c**) are sketches of permissible source region strategy and spectrally resolved measurements, respectively.

the internal bioluminescent source reconstruction, and introduces an efficient iterative shrinkage thresholding method for the large-scale source restoration due to the application of multispectral detection [44, 45]. The algorithm performance and comparison between two sorts of *a priori* knowledge are evaluated with mouse-shaped numerical simulations and *in vivo* heterogeneous small-animal imaging experiments.

This paper is organized as follows. The next section presents the details of two kinds of *a priori* knowledge commonly used in BLT, permissible source region strategy and spectrally resolved method, then an efficient iterative shrinkage thresholding method is introduced for the large-scale inverse source restoration. Bioluminescence tomography-based multimodality imaging prototype system is also simply described in Section 2. In the third section, the performance of the above two *a priori* knowledge is compared with the simulation data based on mouse-shaped atlas and *in vivo* heterogeneous mouse experiments by BLT-based multimodality imaging system. Meanwhile, the reconstruction efficiency and quality are validated using a modified Newton-type optimization approach and the iterative shrinkage thresholding method respectively. Finally, we discuss relevant issues and conclude the paper.

2. Methods and equipments

2.1 Diffusion approximation and Robin boundary condition

In biophotonics, the light transport in the biological tissue can be accurately modelled by the radiative transfer equation (RTE) approximated from Maxwell's equations [42]. However, RTE is extremely computationally burdensome and expensive due to its integrodifferential nature [42, 46, 47]. Generally speaking, analytical solutions of RTE can not be obtained for three-dimensional arbitrarily shaped organisms with complex internal structure [42, 47]. For this issue, high-order approximation models of RTE have been studied and established, such as spherical harmonics (P_N) and discrete ordinates (S_N) equations [47–49]. Based on P_N, simplified spherical harmonics (SP_N) equations have been proposed and used for photon propagation in tissues in the visible and near-infrared spectrum [47, 50, 51]. Moreover, RTE can also been transformed to an integral equation using a generalized delta-Eddington phase function [23, 52]. However, the above transfer models are quite complicated and computationally expensive. Therefore, the widely employed mathematical approximation to RTE is the diffusion equation under the assumption that light scattering dominates over absorption [42, 53, 54]. Considering that the imaging experiment is performed in a light-tight low-background imaging chamber and the internal light source is approximately constant, the propagation of bioluminescent light in tissues can be represented by the following steady-state diffusion equation and Robin boundary condition [11, 17, 20, 54]:

$$-\nabla \cdot (D(\mathbf{r})\,\nabla \Phi(\mathbf{r})) + \mu_a(\mathbf{r})\,\Phi(\mathbf{r}) = S(\mathbf{r}) \tag{1}$$

$$\Phi(\mathbf{r}) + 2A(\mathbf{r}; n, n')\,D(\mathbf{r})\,(\mathbf{v}(\mathbf{r})\,\nabla \Phi(\mathbf{r})) = 0 \tag{2}$$

where $\mathbf{r} \in \Omega$ in Eq. (1) and $\mathbf{r} \in \partial\Omega$ in Eq. (2); Ω and $\partial\Omega$ are the imaging domain and the corresponding boundary respectively; $\Phi(\mathbf{r})$ represents the photon flux density at location $\mathbf{r}$ in W/mm^2; $S(\mathbf{r})$ denotes the internal bioluminescent source density in W/mm^3; $\mu_a(\mathbf{r})$ is the absorption coefficient in mm^{-1}; $D(\mathbf{r}) = (3(\mu_a(\mathbf{r}) + (1-g)\,\mu_s(\mathbf{r})))^{-1}$ is the optical diffusion coefficient, g the anisotropy parameter and $\mu_s(\mathbf{r})$ the scattering coefficient in mm^{-1}; $\mathbf{v}(\mathbf{r})$ refers to the unit normal vector outward to the boundary $\partial\Omega$; $A(\mathbf{r}; n, n')$ is a function to incorporate the mismatch between the refractive indices n within Ω and n' in the surrounding medium.

2.2 Permissible source region and spectrally resolved methods

For permissible source region strategy, using the Galerkin method, Gauss's theorem, and finite element analysis, Eqs. (1) and (2) can be deduced to the following matrix equation linking the internal bioluminescent source distribution to be solved and the boundary measurements [15, 20, 31, 34, 41]:

$$\boldsymbol{\Phi}_{psr}^{meas} = \boldsymbol{A}_{psr}\boldsymbol{S}_{psr} \tag{3}$$

where $\boldsymbol{\Phi}_{psr}^{meas}$ denotes the surface photon density on the measurable node; $\boldsymbol{A}_{psr}$ is a $N_b \times N_p$-order system matrix, N_b the number of boundary measured points and N_p the number of discretized nodes in the permissible source region; $\boldsymbol{S}_{psr}$ represents the light source density in the permissible source region that contains N_p variables.

Comparatively, considering the influence of source spectrum on tissue optical properties, a linear system between the transmitted bioluminescent signals measured on the external surface of the small animal and the internal light source can be obtained in different spectrums using spectrally resolved method [21, 25, 35, 36, 40]:

$$\boldsymbol{\Phi}_{srm}^{meas} = \boldsymbol{A}_{srm}\boldsymbol{S}_{srm} \tag{4}$$

where

$$\boldsymbol{\Phi}_{\text{srm}}^{\text{meas}} = \begin{bmatrix} \boldsymbol{\Phi}_{\text{srm},1}^{\text{meas}} \\ \boldsymbol{\Phi}_{\text{srm},2}^{\text{meas}} \\ \vdots \\ \boldsymbol{\Phi}_{\text{srm},K}^{\text{meas}} \end{bmatrix}, \qquad \boldsymbol{A}_{\text{srm}} = \begin{bmatrix} \zeta_1 \boldsymbol{A}_{\text{srm},1} \\ \zeta_2 \boldsymbol{A}_{\text{srm},2} \\ \vdots \\ \zeta_K \boldsymbol{A}_{\text{srm},K} \end{bmatrix} \tag{5}$$

K denotes the number of spectra divided by filters; $\boldsymbol{\Phi}_{\text{srm},\xi}^{\text{meas}}$ is the measured data in the ξ-th spectral band $[\lambda_\xi, \lambda_{\xi+1}]$, $\xi = 1, 2, \cdots, K$; ζ_ξ refers to the energy contribution of internal light source in $[\lambda_\xi, \lambda_{\xi+1}]$; $\boldsymbol{A}_{\text{srm},\xi}$ represents a N_n-order matrix, and N_n is the total number of discretized points in the entire domain Ω; $\boldsymbol{S}_{\text{srm}}$ is the source densities on N_n scattering nodes. From the above analysis, we can see that Eq. (4) becomes a large-scale linear inverse problem because the $(KN_n) \times N_n$ matrix $\boldsymbol{A}_{\text{srm}}$ is much larger than $\boldsymbol{A}_{\text{psr}}$ in Eq. (3). Therefore, we should find an efficient algorithm to solve $\boldsymbol{S}_{\text{srm}}$.

In general, $\boldsymbol{A}_{\text{psr}}$ and $\boldsymbol{A}_{\text{srm}}$ are ill-conditioned, so the regularization method should be performed to stabilize the solution. The ill-posed Eq. (3) will be converted into a closely well-posed equation whose solution is the optimal approximation to the true source with the help of a regularization term [20, 29, 34, 44, 45, 55]. For Eq. (4), the same processing should be exerted. Heretofore, Tikhonov regularization is a widely used method for ill-posed problem by adding a quadratic penalty to the objective function, which is called as l_2-based regularization [44, 45]. However, this method is oversmoothed for the solution and the high-frequency information of the surface measurements is usually ignored [6, 45, 55]. Considering the sparse representation of the internal light source, the following l_1 norm regularization criterion is employed for BLT reconstruction. Furthermore, l_1 regularization is less sensitive to outliers compared with l_2-based regularization [44, 45],

$$\min \left\{ F(\boldsymbol{S}) \equiv \left\| \boldsymbol{A}\boldsymbol{S} - \boldsymbol{\Phi}^{\text{meas}} \right\|^2 + \alpha \left\| \boldsymbol{S} \right\|_1 \right\} \tag{6}$$

where $\boldsymbol{S}$ represents $\boldsymbol{S}_{\text{psr}}$ in Eq. (3) or $\boldsymbol{S}_{\text{srm}}$ in Eq. (4); $F(\boldsymbol{S})$ stands for the objective function; $\boldsymbol{A}$ and $\boldsymbol{\Phi}^{\text{meas}}$ denote the system matrices and measured vectors in permissible source region strategy and spectrally resolved method respectively; α is the regularization parameter.

2.3 *Efficient bioluminescence tomography method*

Considering the large-scale characteristic of the above unresolved problem, an efficient iterative shrinkage thresholding method is employed to determine the internal bioluminescent source distribution [44, 45]. The conventional iterative shrinkage thresholding method for solving Eq. (6) is given by [44, 45, 56]:

$$\boldsymbol{S}_k = \Gamma_{\alpha t}(\boldsymbol{S}_{k-1} - 2t\boldsymbol{A}^T(\boldsymbol{A}\boldsymbol{S}_{k-1} \boldsymbol{\Phi}^{\text{meas}})) \tag{7}$$

where t is the step size and $\Gamma_\zeta : \mathbb{R}^n \to \mathbb{R}^n$ denotes the shrinkage function defined as:

$$\Gamma_\zeta(\boldsymbol{S}) = (|\boldsymbol{S} - \zeta|) + \text{sgn}\,(\boldsymbol{S}) \tag{8}$$

where sgn $(\cdot)$ represents the sign function. The basic iteration step of the above method can be simply expressed as:

$$\boldsymbol{S}_k = \Gamma_{\alpha t}(\boldsymbol{S}_{k-1}) \tag{9}$$

This method has been widely studied and utilized in signal and image processing due to its simplicity and ability to solve large-scale problems even with the dense sensitivity matrix [44, 45, 56]. However, the convergence rate of this algorithm is quite slow and unbearable for practical application that should be improved, so the efficient iterative shrinkage thresholding method is employed to accelerate the optimization, in which the iterative source reconstruction can be carried out with the help of an intermediate variable [44, 45]:

$$\boldsymbol{S}_k = p_L(\boldsymbol{T}_k) \tag{10}$$

where $\boldsymbol{T}_k$ depicts the intermediate variable that can be computed by the following formula when $k \geq 2$ [45]:

$$\boldsymbol{T}_k = \boldsymbol{S}_{k-1} + \left(\frac{t_{k-1} - 1}{t_k} \right) (\boldsymbol{S}_{k-1} - \boldsymbol{S}_{k-2}) \tag{11}$$

$$t_k = \frac{1 + \sqrt{1 + 4t_{k-1}^2}}{2} \tag{12}$$

where $\boldsymbol{S}_0$ represents the initial iteration value, $\boldsymbol{T}_1 = \boldsymbol{S}_0$ and $t_1 = 1$. The minimum operator p_L in Eq. (10) is defined as follows [45]:

$$p_L(\boldsymbol{T}) = \arg\min_{\boldsymbol{S}} \left\{ \alpha \left\| \boldsymbol{S} \right\|_1 + \frac{L}{2} \left\| \boldsymbol{S} - \left(\boldsymbol{T} - \frac{1}{L} \nabla \left\| \boldsymbol{A}\boldsymbol{T} - \boldsymbol{\Phi}^{\text{meas}} \right\|^2 \right) \right\|^2 \right\} \tag{13}$$

where L is the Lipschitz constant of $\nabla \left\| \boldsymbol{A}\boldsymbol{T} - \boldsymbol{\Phi}^{\text{meas}} \right\|^2$ and the smallest value of L is double of the largest eigenvalue of the matrix $\boldsymbol{A}^T\boldsymbol{A}$.

After several periodic iterations of Eqs. (10), (11), (12), and (13), the sequence $\boldsymbol{S}_k$ can converge to an optimal solution $\boldsymbol{S}$ that is the internal bioluminescent source need to be reconstructed.

To sum up, the flowchart of the above two *a priori* knowledge-based algorithms, permissible source region strategy and spectrally resolved meas-

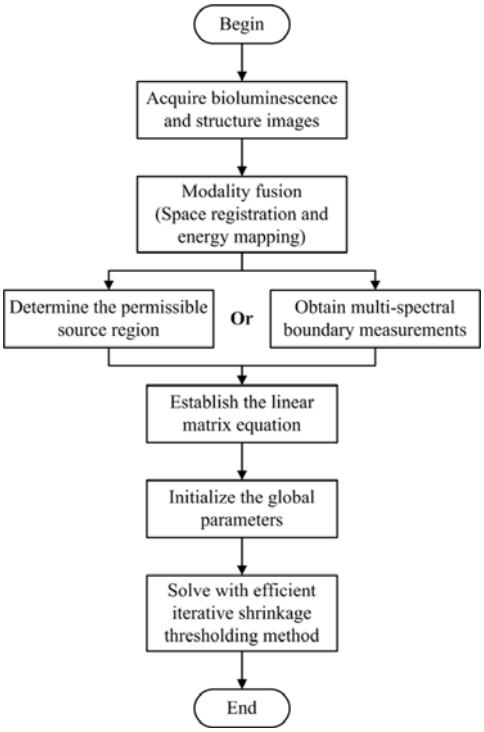

Figure 2 The data processing flowchart used in this contribution.

urements, with efficient iterative shrinkage thresholding method is shown in Figure 2.

2.4 Bioluminescence tomography-based multimodality imaging system

In order to validate the performance of the reconstruction methods, a bioluminescence tomography-based multimodality imaging system was constructed by our group, as shown in Figure 3 [30, 57]. The multimodality imaging prototype system can perform micro-CT imaging, multiview and multispectral bioluminescence imaging. The micro-CT imaging system consists of a microfocus X-ray source tube (UltraBright, Oxford Instruments, USA), a X-ray flat panel detector (C7942CA-02, Hamamatsu, Japan), a frame grabber card (IMAQ PCI-1424, National Instruments, USA), two motorized translation stages (PSA200-11, Zolix Instruments, P.R. China), and a motorized rotation stage (RAK-100, Zolix Instruments, P.R. China). The spatial resolution of the micro-CT imaging system is up to 14.5 lp/mm and a 100 μm^3 voxel size is often adopted in multimodality imaging experiment, which is high enough to provide the surface topography and anatomical structure information of the small animal for optical tomography whose spatial resolution is about in the magnitude of millimeter and submillimeter. The large field of view (FOV) of the micro-CT system allows nearly the whole body imaging of a normal-size mouse to be acquired in a single scan that usually takes less than ten minutes. The optical imaging system is mainly composed of a liquid-nitrogen-cooled backilluminated CCD camera (VersArray 1300B, Princeton Instruments, USA), a focus lens (Nikkor 17–55 mm f/2.8, Nikon, Japan) and a light-tight enclosure (not shown in Figure 3). The CCD array can generate 1340×1300 pixels and 16 bits dynamic range image with 20×20 μm sized pixel. The dark current of the camera is reduced largely through cooling the CCD chip down to $-110\,^{\circ}C$ using liquid nitrogen, which makes it more suitable for long-time exposure. Furthermore, the quantum efficiency (QE) of the CCD camera is greater than 80% for the wavelength range between 500 nm and 700 nm. With the motorized rotation stage used in the micro-CT imaging system, multiview bioluminescent light distribution on the small animal surface can be captured. Furthermore, in order to reduce the ill-posedness of BLT, multispectral source reconstruction has attracted remarkable attention and a consensus that spectrally resolved method can enhance the uniqueness and stability of BLT solution has been achieved [21, 40]. Thus, a set of bandpass or cutoff filters are utilized for multispectral or quasispectral measurements [40]. In addition, considering the nonuniformity of pixels, the CCD camera should be calibrated by an integrating sphere 12 inches in diameter (USS-1200V-LL Low-Light Uniform Source, Labsphere, North Sutton, NH) [32]. Multiview overlaid images of photographs and luminescent distribution can be acquired by the CCD camera from four directions with 90 degrees intervals, which can increase surface measurements of the small animal for inverse source restoration.

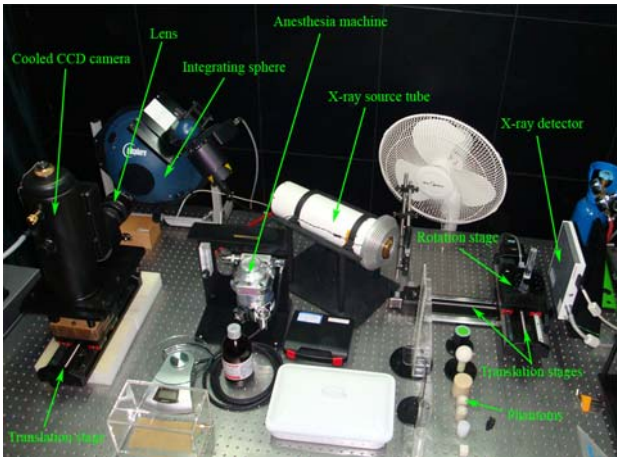

Figure 3 (online color at: www.biophotonics-journal.org) Bioluminescence tomography-based multimodality imaging system.

3. Experiments and results

3.1 Mouse-shaped numerical experiments

In order to compare spectrally resolved information and permissible source region strategy for inverse bioluminescence source recovery, a three-dimensional mouse atlas was applied to provide irregular-shaped reconstruction domain with complex internal structure, which was acquired using the aforementioned micro-CT imaging system. The anatomical structure information was acquired using our micro-CT imaging system with a Feldkamp–Davis–Kress (FDK) filtered backprojection algorithm accelerated by a graphics processing unit (GPU) and segmented with the interactive method [58–61]. The corresponding anatomical structure data can be downloaded free from http://www.mosetm.net. The segmented organs mainly contained five kinds of tissue, namely, lungs, muscle, heart, bone, and liver, so the torso of a mouse-shaped phantom was employed for the following bioluminescence tomography numerical experiments, as shown in Figure 4a. Furthermore, the mouse-shaped phantom was discretized into volumetric mesh for finite-element-based reconstruction, and it consisted of 2579 nodes and 13200 tetrahedra with 1390 surface triangular elements, as presented in Figure 4b. A light source with 0.663 mm^3 volume was embedded into the mouse-shaped phantom with its center at (22.88, 28.93, 12.86) mm, as shown in Figure 4a. In addition, the bioluminescent light exitance map on the mouse-shaped phantom surface was obtained using Monte Carlo method-based molecular optical simulation environment (MOSE) developed by our group, which is a general simulation platform of forward problem for photon propagation in the biological tissue [62, 63].

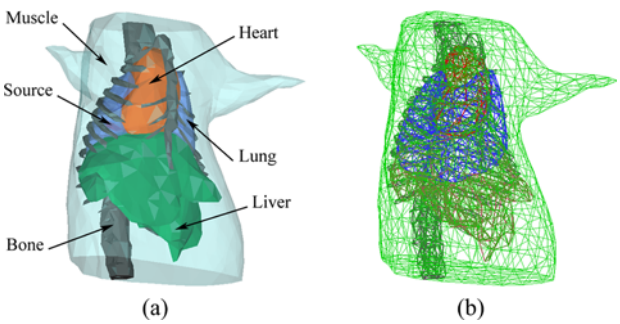

Figure 4 (online color at: www.biophotonics-journal.org) Mouse-shaped phantom developed by micro-CT imaging system. (**a**) Mouse-shaped phantom with different segmented organs and light source; (**b**) Volumetric mesh used in inverse source reconstruction.

3.1.1 Reconstruction using permissible source region strategy

For permissible source region strategy, *a priori* optical properties of each organ in the whole spectrum were specified according to the document [64] and references therein, as listed in Table 1. Considering the severely ill-posed characteristic of BLT, *a priori* permissible source region was determined based on the surface light power distribution to enhance the uniqueness and stability of BLT solution. The permissible source region in this experiment was initially specified as:

$$\mathrm{PS1} = \{(x,y,z) \mid 21 < y < 31{,}7 < z < 17, (x,y,z) \in \Omega\}.$$

The volume ratio of the above permissible source region and the whole domain was about 8.73%, and the position of the corresponding reconstructed source was located at (22.98, 30.58, 12.99) mm using the efficient iterative shrinkage thresholding method, as shown in Figure 5a. The actual source was embedded in the phantom with its center at (22.88, 28.93, 12.86) mm, and the Euclidean distance between the actual source and recovered result was 1.659 mm, which was computed by the formula: $Ed_{\mathrm{error}} = \|\mathbf{r}_{\mathrm{actual}} - \mathbf{r}_{\mathrm{recons}}\|_2$, where $\mathbf{r}_{\mathrm{actual}}$ and $\mathbf{r}_{\mathrm{recons}}$ denote the positions of the actual and reconstructed sources, respectively. Moreover, the other two experiments were performed to demonstrate the effect of the permissible source region size on the reconstruction quality, and the computational results are showed in Figures 5c and e. The corresponding permissible source regions were defined as follows:

$$\mathrm{PS2} = \{(x,y,z) \mid 24 < y < 34{,}8 < z < 17, (x,y,z) \in \Omega\}.$$

$$\mathrm{PS3} = \{(x,y,z) \mid 23 < y < 33{,}7 < z < 18, (x,y,z) \in \Omega\}.$$

All of the above results were computed through efficient iterative shrinkage thresholding method and the minimum energy function Eq. (6). Furthermore, a modified Newton-type optimization method was also employed for the linear inverse problem Eq. (3) to illustrate the higher efficiency of the reconstruction algorithm used in this contribution, and the ex-

Table 1 Optical parameters for each organ of mouse-shaped phantom (units of μ_a and μ_s: mm^{-1}).

Organ	Lung	Muscle	Heart	Bone	Liver
μ_a	0.010	0.350	0.200	0.002	0.035
μ_s	4.000	23.000	16.000	20.000	6.000
g	0.900	0.940	0.850	0.900	0.900

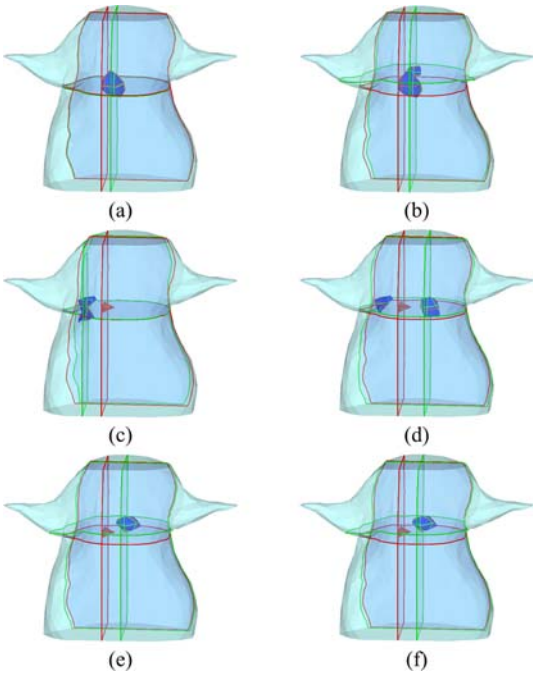

Figure 5 (online color at: www.biophotonics-journal.org) Reconstructions in numerical experiments using EIST and MNO based on different permissible source regions. (**a**) PS1 by EIST; (**b**) PS1 by MNO; (**c**) PS2 by EIST; (**d**) PS2 by MNO; (**e**) PS3 by EIST; (**f**) PS3 by MNO. The internal red region and blue domain represent the actual source and recovered result separately. Cross sections with red and green boundaries are the center positions of actual and reconstructed sources, respectively. PS1, PS2, PS3, and the quantitative comparison are shown in Table 2.

perimental results are also listed in Figures 5b, 5d, 5f, and Table 2. All reconstructions were performed on a personal computer with an Intel Core 2 Duo 2.40 GHz CPU and 2 GB RAM. From the experimental data in Table 2, we can see that the efficient iterative shrinkage thresholding method not only has faster global convergence rate, but also has better reconstruction accuracy in comparison with modified Newton-type optimization approach. For the sake of convenience, EIST represents the efficient iterative shrinkage thresholding algorithm, and MNO indicates the modified Newton-type optimization method in this section.

3.1.2 Reconstruction with spectrally resolved measurements

During spectrally resolved measurement, the whole spectrum was divided into three bands: [575, 625] nm, [625, 675] nm and [675, 725] nm, so that the multispectral surface bioluminescent light distribution could be obtained. The corresponding energy contribution of the internal light source and the optical properties in each spectral band are listed in Table 3, which can refer to the Ref. [64]. In order to illuminate the importance of the boundary measurement data quantity, different combinations of separated spectra were used to recover the internal light source. The reconstruction results are shown in Figures 6a–f and Table 4. In Table 4, the computational

Table 2 Reconstruction results using permissible source region strategy for mouse-shaped phantom.

Region	Volume Ratio	Method	Recons. Position (mm)	Location Error (mm)	Recons. Time (s)
PS1 $= \{(x,y,z) \mid 21 < y < 31,$ $7 < z < 17, (x,y,z) \in \Omega\}$	8.73%	MNO	(23.29, 30.94, 10.58)	3.070	8.106
		EIST	(22.98, 30.58, 12.99)	1.659	6.734
PS2 $= \{(x,y,z) \mid 24 < y < 34,$ $8 < z < 17, (x,y,z) \in \Omega\}$	10.11%	MNO	(22.21, 33.54, 12.38)	4.681	26.672
		EIST	(23.70, 25.55, 12.84)	3.479	10.859
PS3 $= \{(x,y,z) \mid 23 < y < 33,$ $7 < z < 18, (x,y,z) \in \Omega\}$	12.55%	MNO	(22.48, 32.28, 11.18)	3.766	41.672
		EIST	(22.48, 32.28, 11.18)	3.766	14.641

Table 3 Optical properties of mouse-shaped phantom in each spectrum (units of μ_a and μ_s': mm^{-1}).

Organ	[575, 625] nm		[625, 675] nm		[675, 725] nm	
	μ_a	μ_s'	μ_a	μ_s'	μ_a	μ_s'
Source ratio	0.38		0.43		0.19	
Lung	0.0707	2.305	0.0195	2.209	0.0125	2.124
Muscle	0.0317	0.586	0.0089	0.467	0.0063	0.379
Heart	0.0218	1.129	0.0064	1.007	0.0052	0.905
Bone	0.0024	2.935	0.0009	2.609	0.0011	2.340
Liver	0.1275	0.761	0.0329	0.700	0.0176	0.648

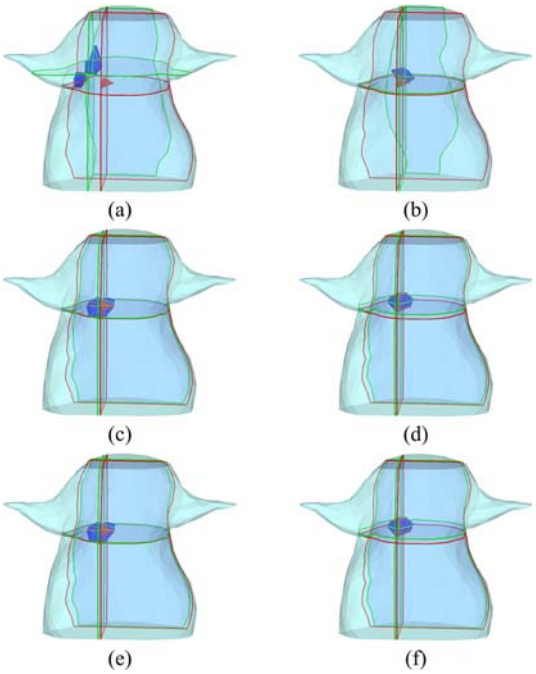

Figure 6 (online color at: www.biophotonics-journal.org) The reconstructed results in numerical experiments by EIST and MNO using different multispectral information. (**a**) Single spectrum by EIST; (**b**) Single spectrum by MNO; (**c**) Two spectra by EIST; (**d**) Two spectra by MNO; (**e**) Three spectra by EIST; (**f**) Three spectra by MNO. The internal red region and blue domain represent the actual source and recovered result separately. Cross sections with red and green boundaries are the center positions of actual and reconstructed sources, respectively.

time and reconstructed position were compared between EIST and MNO. We can draw the conclusion that the reconstruction quality is improved largely with the increase of boundary measurements, namely, the number of spectra. However, the distance error between the reconstructed source and the actual one does not reduce unceasingly when the number of spectra reaches a certain threshold, but the computational efficiency is greatly degraded.

3.1.3 Reconstruction with different source locations and noise levels

As is known, the effectiveness and feasibility of the inversion reconstruction can be better verified by the mouse-shaped numerical experiments with different source locations and noise levels. Therefore, we performed several numerical simulations using diverse permissible source regions and combination spectra based on different source locations and noise levels. In the experiments, white Gaussian noise with different levels was added to the bioluminescence signal detected on the mouse-shaped phantom surface. The corresponding reconstructed results are summarized in Table 5, and we can see that the reconstructions with low-level noise are better than those with high-level noise. Moreover, the location of the internal light source has little impact on the reconstruction result.

3.2 In vivo mouse experiments

In order to further compare the performance of different *a priori* knowledge, *in vivo* mouse heterogeneous imaging experiment was carried out using the aforementioned bioluminescence tomography-based multimodality imaging prototype system. Before the imaging experiment, exogenous contrast agent Fenestra LC (ART, Montreal, Canada) was slowly injected into a 21 g weight nude mouse (Nu/Nu, Laboratory Animal Center, Peking University, P.R. China) after 24 h fasting at a dose of 15 ml/kg over a period of 30–60 s via the lateral tail vein to enhance the contrast resolution of soft tissues in the CT image. During the whole imaging experiment, the mouse was anesthetized with intraperitoneal injection of 0.16 ml 13% aqueous urethane. A catheter of 1.5 mm diameter and 2.5 mm length filled with peroxide, ester compound, and fluorescent dye after thorough mix was transplanted into the liver interspace of the nude mouse. The catheter with luminescent liquid was chosen as the internal bioluminescent

Table 4 The reconstructed results based on multispectral information for mouse-shaped phantom.

Spectrum	Method	Recons. Position (mm)	Location Error (mm)	Recons. Time (s)
Single	MNO	(26.63, 29.45, 12.60)	3.793	25259.38
	EIST	(25.83, 26.59, 9.41)	5.113	49.172
Two	MNO	(23.48, 28.55, 12.04)	1.089	20322.58
	EIST	(23.63, 28.40, 12.79)	0.923	100.437
Three	MNO	(23.48, 28.55, 12.04)	1.089	20495.16
	EIST	(23.63, 28.40, 12.79)	0.923	166.422

Table 5 Quantitative comparison of reconstruction results with different source locations and noise levels.

Source Position (mm)	Method	Region or Spectrum	Noise Level	Recons. Position (mm)	Location Error (mm)
(22.88, 28.93, 12.86)	Permissible Source Region	PS = $\{(x,y,z) \mid 21 < y < 31, 7 < z < 17, (x,y,z) \in \Omega\}$	10%	(22.99, 30.58, 12.99)	1.661
			50%	(24.75, 30.89, 14.73)	3.296
(18.37, 32.93, 14.04)	Permissible Source Region	PS = $\{(x,y,z) \mid 29 < y < 38, 7 < z < 18, (x,y,z) \in \Omega\}$	10%	(17.28, 31.67, 15.26)	2.065
			50%	(15.79, 31.87, 16.49)	3.717
(22.88, 28.93, 12.86)	Spectrally resolved Measurements	Two Spectra	10%	(23.63, 28.40, 12.79)	0.925
			50%	(22.99, 30.58, 12.99)	1.661
(18.37, 32.93, 14.04)	Spectrally resolved Measurements	Three Spectra	10%	(18.11, 33.13, 15.28)	1.285
			50%	(15.88, 33.26, 16.58)	3.574

source because its emission spectrum is close to the wavelength range of the luciferase. Four views of bioluminescent light distribution on the mouse surface were acquired by the above optical imaging system, and the exposure time of each view was set to 60 s, as shown in Figure 7a. The corresponding four photographic images were recorded using the same optical imaging system with an exposure time of 2 s, which could be used for the image registration between bioluminescence and CT. The typical photographic image is showed in Figure 7b. Moreover, spectrally resolved photon energy distributions were also collected in three spectra: [600, 650] nm, [650, 700] nm, and [700, 760] nm, and the corresponding energy percentages of the internal light source in each spectrum were measured by a spectrometer as follows: $\varpi_1 = 0.36$, $\varpi_2 = 0.48$, and $\varpi_3 = 0.16$. From the above depiction, the total time used for luminescent light acquisition can be expressed as follows:

$$t_{\text{total}} = 4 \times 3 \times 60\ \text{s} = 720\ \text{s}\,.$$

In addition, we have measured the light signal emitting from the above luminescent solutions at different times, and then the decay curve could be determined, as shown in Figure 8. The vertical axis shows the gray value of the pixel, and the abscissa represents time. From the decay curve in the figure, we can see that the lifetime of luminescent solutions is longer than the total time for luminescent light acquisition, so multiview and multispectral data acquisition can be successfully completed.

Then, the anesthetized mouse was scanned by the micro-CT imaging system to provide three-dimensional geometric shape and anatomic structure information for inverse source reconstruction. The voltage of the X-ray tube was specified as 50 kVp

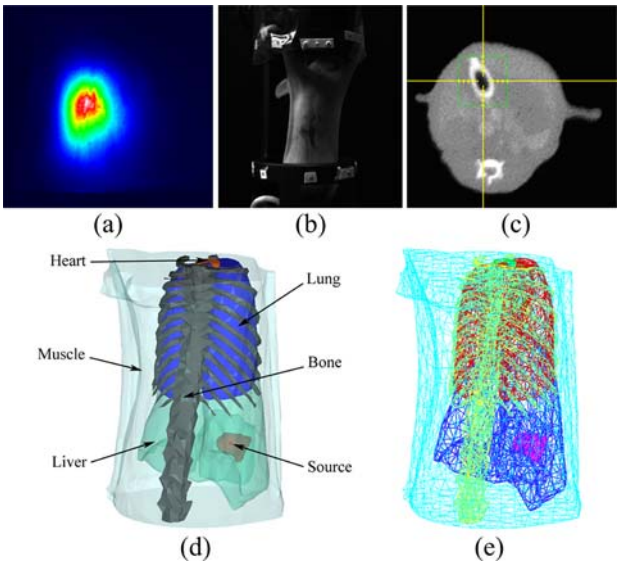

Figure 7 (online color at: www.biophotonics-journal.org) (**a**) The bioluminescent image captured by the cooled CCD camera; (**b**) The photographic image; (**c**) A reconstruction slice using micro-CT; (**d**) The segmented heterogeneous mouse model; (**e**) The volumetric mesh used in source restoration.

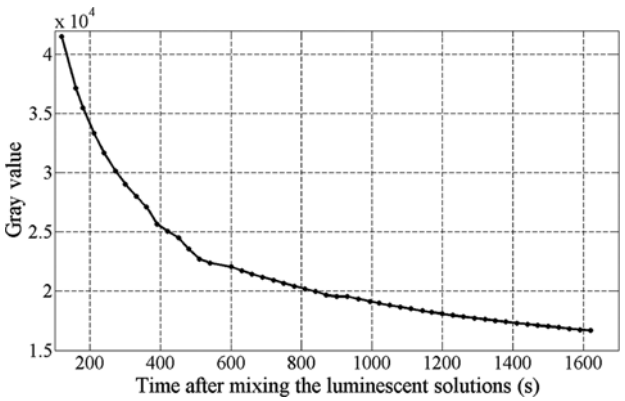

Figure 8 The decay curve of mixed luminescent solutions.

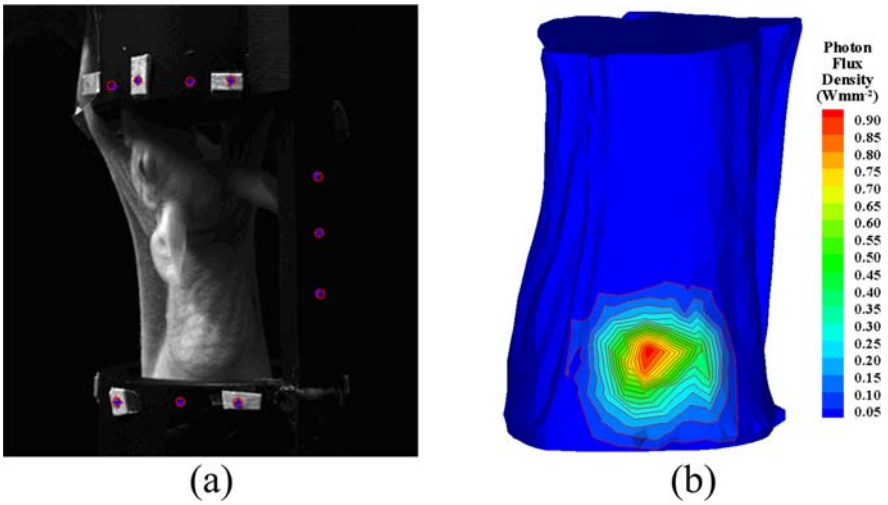

Figure 9 (online color at: www.biophotonics-journal.org) (**a**) The registration result of optical and micro-CT data, magenta circles and blue stars indicate the positions of the registration points in optical and CT data, respectively; (**b**) The surface bioluminescent light distribution.

with 1 mA current, and an aluminum board of 0.5 mm thickness was used to filter the soft X-rays. In the micro-CT imaging experiment, the detector was set to 2×2 binning model and 360 projection views of 1120×1172 size were acquired with 0.467 s integrated time, and Figure 7c depicts a certain reconstruction slice of the mouse. After fast cone-beam CT image reconstruction, interactive segmentation was performed to obtain the heterogeneous mouse model, which was further discretized into a volumetric mesh for finite-element-method-based bioluminescence tomography. Figures 7d and 7e illustrate the segmented mouse model and the corresponding tetrahedral-element mesh, respectively. The spatial registration of micro-CT data and photographic images was accomplished according to the markers preset on the mouse holder, and then the two-dimensional bioluminescent light distribution was mapped to the three-dimensional volumetric mesh. Figure 9a shows the spatial registration result of the above two modalities, and Figure 9b represents the light exitance map on the torso surface in view of the implanted source being near the liver of the mouse.

3.2.1 Reconstruction using permissible source region strategy

Before inverse source reconstruction, the optical properties of each organ for the whole spectrum and the discrete spectra were determined according to the methods in Refs. [64, 65], as listed in Table 6. In the study of permissible source region strategy, the initial region of interest was set as the following domain based on surface light distribution:

$$\mathrm{PS1} = \{(x,y,z) \mid 18 < x < 27, 13 < y < 19, \\ 3 < z < 11, (x,y,z) \in \Omega\}.$$

The corresponding reconstructed results are shown in Figures 10a and 10b. Subsequently, the permissible source region was expanded gradually, and the recovered source and computation time are summarized in Figures 10c–f and Table 7. PS2 and PS3 were separately specified as:

$$\mathrm{PS2} = \{(x,y,z) \mid 17 < x < 28, 12 < y < 20, \\ 2 < z < 12, (x,y,z) \in \Omega\},$$

$$\mathrm{PS3} = \{(x,y,z) \mid (x,y,z) \in \Omega\}.$$

Table 6 Optical parameters of each mouse organ in whole and divided spectra (units of μ_a and μ_s': mm^{-1}).

Organ	Whole		[600, 650] nm		[650, 700] nm		[700, 760] nm	
	μ_a	μ_s'	μ_a	μ_s'	μ_a	μ_s'	μ_a	μ_s'
Lung	0.071	2.305	0.993	0.731	0.313	0.668	0.165	0.620
Muscle	0.075	2.178	0.166	1.068	0.052	0.945	0.028	0.853
Heart	0.022	1.129	0.244	0.527	0.077	0.413	0.040	0.337
Bone	0.032	0.586	0.170	2.775	0.054	2.444	0.028	2.201
Liver	0.128	0.646	0.549	2.259	0.174	2.157	0.090	2.077

Table 7 The reconstruction results using permissible source region strategy for in vivo mouse experiment.

Region	Volume Ratio	Method	Recons. Position (mm)	Location Error (mm)	Recons. Time (s)
PS1 = $\{(x,y,z) \mid 18 < x < 27,$ $13 < y < 19{,}3 < z < 11, (x,y,z) \in \Omega\}$	1.17%	MNO	(25.15, 14.92, 7.41)	2.879	0.047
		EIST	(25.97, 18.95, 8.24)	0.604	1.156
PS2 = $\{(x,y,z) \mid 17 < x < 28,$ $12 < y < 20{,}2 < z < 12, (x,y,z) \in \Omega\}$	2.76%	MNO	(20.79, 17.90, 5.69)	3.132	0.188
		EIST	(26.46, 19.96, 10.15)	1.653	1.922
PS3 = $\{(x,y,z) \mid (x,y,z) \in \Omega\}$	100%	MNO	(25.15, 14.92, 7.41)	2.879	256216.9
		EIST	(21.37, 16.55, 7.92)	2.605	145.172

From Table 7, it can be seen that the location error becomes larger, comparatively, the reconstruction efficiency decreases greatly when the volume of the permissible source region increases step by step. Furthermore, from the above experimental results, we can also find that EIST is faster than MNO by several orders of magnitude, especially for large-scale problems. However, it should be noted that the EIST algorithm is not dominant compared with MNO method in some small-scale optimization calculations.

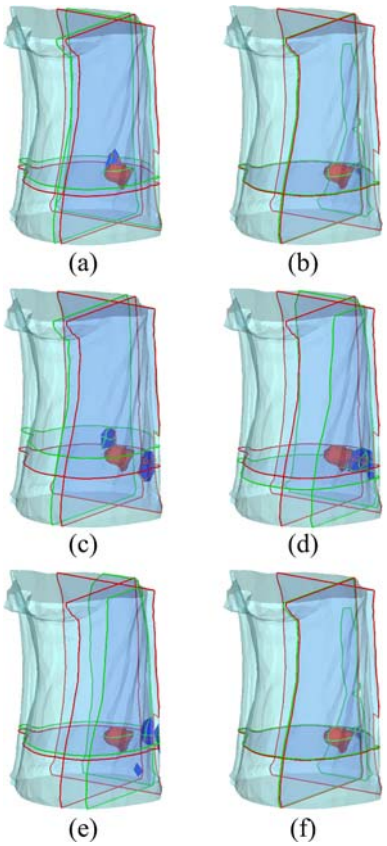

Figure 10 (online color at: www.biophotonics-journal.org) The recovered sources by EIST and MNO using different permissible source regions. (**a**) PS1 by EIST; (**b**) PS1 by MNO; (**c**) PS2 by EIST; (**d**) PS2 by MNO; (**e**) PS3 by EIST; (**f**) PS3 by MNO. The internal red region and blue domain represent the actual source and recovered result separately. Cross sections with red and green boundaries are the center positions of actual and reconstructed sources, respectively. PS1, PS2, PS3, and the quantitative comparison are illuminated in Table 7.

3.2.2 Reconstruction with spectrally resolved measurements

Similarly, single, two, and three spectra boundary measured data were employed for inverse source reconstruction respectively. Figures 11a–f and Table 8 compare the corresponding reconstruction results and computational efficiencies. It is worth mentioning that the conventional MNO method is too slow for practical applications because the fusion of multispectral information largely increases the amount of the known data besides reducing the ill-posedness of BLT. However, efficient iterative shrinkage thresholding method can determine the internal bioluminescent source in the anesthetized mouse efficiently. In order to illuminate the difference of reconstruction performance between EIST and MNO more obviously, all the computational time and location error in mouse-shaped numerical and *in vivo* experiments are dotted in Figures 12a and 12b, respectively. In Figure 12, the blue and red lines represent the computational results based on the permissible source region and multispectral measurements, respectively. The points and crosses on the lines denote the reconstructions using MNO and EIST separately. From Figure 12a, we can see that the computational efficiency of EIST is higher than that of MNO, except for a few small-scale source reconstructions like PS1 and PS2 cases in *in vivo* mouse experiment, whose volume ratios are only 1.17% and 2.76%, respectively. In addition, the permissible source region method requires much less computational time than spectrally resolved-based algorithm in view of the reduction of variables to be solved and without consideration of multispectral measurements. From Figure 12b, the reconstructed precision of EIST is generally higher than that of MNO, and the recon-

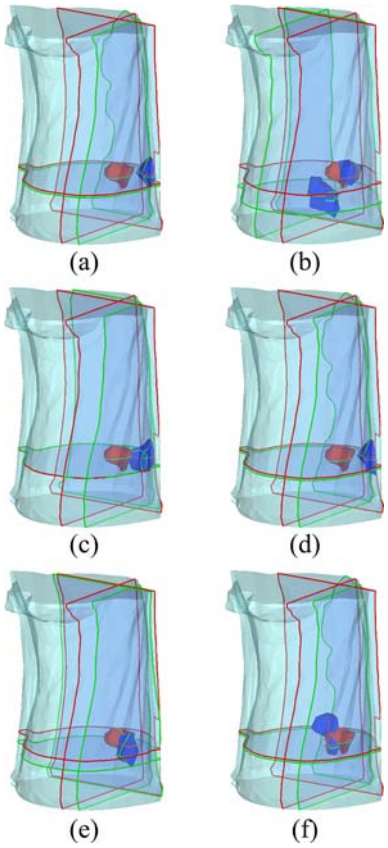

Figure 11 (online color at: www.biophotonics-journal.org) The recovered sources by EIST and MNO using different spectra. (**a**) Single spectrum by EIST; (**b**) Single spectrum by MNO; (**c**) Two spectra by EIST; (**d**) Two spectra by MNO; (**e**) Three spectra by EIST; (**f**) Three spectra by MNO. The internal red region and blue domain represent the actual source and recovered result separately. Cross sections with red and green boundaries are the center positions of actual and reconstructed sources, respectively.

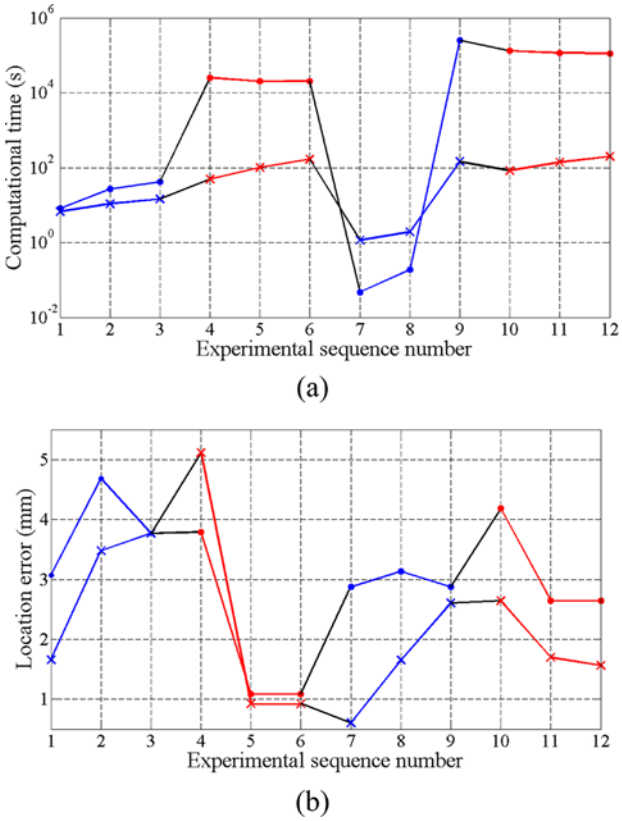

Figure 12 (online color at: www.biophotonics-journal.org) Comparison of reconstruction performance between MNO and EIST. (**a**) Computational time comparison; (**b**) Location error comparison. The blue and red lines represent the computational results based on the permissible source region and multispectral measurements respectively. The points and crosses on the lines denote the reconstructions using MNO and EIST separately.

struction using spectrally resolved measurements can yield the desired results with smaller location error than the permissible source region-based method, especially for the case of larger *a priori* domain determined before the inversion scheme.

4. Discussion and conclusion

As a novel optical molecular imaging modality, bioluminescence tomography can quantitatively obtain the distribution information of the internal light source, which can *in vivo* reflect the physiological and pathological change processes of the molecular

Table 8 Quantitative comparison of different spectrum composition for in vivo mouse experiment.

Spectrum	Method	Recons. Position (mm)	Location Error (mm)	Recons. Time (s)
Single	MNO	(29.50, 19.28, 4.45)	4.181	132323.1
	EIST	(22.52, 15.61, 7.00)	2.641	83.172
Two	MNO	(22.52, 15.61, 7.00)	2.641	115837.8
	EIST	(21.62, 18.44, 7.33)	1.697	140.109
Three	MNO	(22.52, 15.61, 7.00)	2.641	112915.9
	EIST	(22.53, 20.52, 5.87)	1.562	198.766

targets marked by a certain sensitive and specific bioluminescent reporter luciferase. In comparison with the bioluminescence imaging technology that is generally used for qualitative analysis, bioluminescence tomography can not only carry out quantitative and localization analyses of the internal light source, but can also improve imaging spatial resolution. More importantly, the depth parameter of the reconstructed target in which biomedical researchers are interested can be solved. However, three-dimensional bioluminescence tomography is ill-posed severely because of complex photon propagation in the biological tissue and limited noisy boundary measurement data. Therefore, sufficient *a priori* knowledge should be incorporated to reduce the ill-posedness in inverse source reconstruction and ensure the uniqueness and stability of the bioluminescent solution. In the practical inversion scheme, reducing the unknown variables and increasing the amount of known data are two kinds of commonly used methods. This paper compares the above two methods using mouse-shaped phantom simulation and *in vivo* mouse experiments, and then an efficient iterative shrinkage thresholding inversion algorithm is introduced for a large increase in size of boundary data sets due to the application of multispectral information.

The application of the permissible source region in inverse source reconstruction is an effective strategy to transform the ill-conditioned problem to well-posedness through reducing the number of variables to be solved. Before source reconstruction, the permissible source region must be determined according to *a priori* knowledge of the surface light power distribution and other specific biomedical application. Furthermore, the permissible source region should be sufficiently large in order to contain all the internal light sources. However, the permissible source region can not be easily inferred when the sources approximately locate at half-radius or deeper from the surface due to the heterogeneity of the small animal. In addition, from numerical and *in vivo* experiments, we find that the smaller the permissible source region, the more accurate the source position reconstruction. When the permissible source region becomes larger, the error of the reconstructed source will be more significant. In other words, the size of permissible source region has an important effect on numerical stability and efficiency. On the other hand, the acquisition of multispectral information increases the amount of known boundary measurements that can effectively reduce the ill-posedness of the inverse problem. The application of multispectral data can not only improve the reconstruction largely, but can also detect multiple markers simultaneously. However, the increase of the known data also reduces the reconstruction efficiency because the dimension of the Jacobian matrix becomes very large for most of iteration-based algorithms. Therefore, the study of fast inversion methods is becoming more urgent and has great significance for the application of multispectral information and noncontact detection. To sum up, the permissible source region and multispectral measurements can both reduce the ill-posed nature of bioluminescence tomography and improve the reconstruction. Although the permissible source region method and spectrally resolved-based algorithm can reduce the ill-posedness of BLT and improve the inverse source reconstruction, these two strategies have their own disadvantages. For example, the correct domain of the internal light source may be missing in the selection of the permissible source region due to the heterogeneity of the small animal. The efficiency of the spectrally resolved-based method is reduced due to the acquisition of multispectral data and the increase in the number of boundary measurements. In addition, the extra noise will also be introduced in the long-time collection of bioluminescent light signal. Finally, it is worth mentioning that the permissible source region and multispectral measurements can be combined to further reduce the ill-posed nature of BLT. The application of the permissible source region can improve the efficiency of the spectrally resolved-based method by reducing the number of unknowns to be solved. Similarly, the integration of multispectral information can expand the size of the selected region and enhance the applicability of the permissible source region-based method, especially for the case of a larger *a priori* domain.

This contribution compares the permissible source region strategy and spectrally resolved measurements for bioluminescent source recovery, and introduces an efficient iterative shrinkage thresholding method for the large-scale source reconstruction. The mouse-shaped numerical simulation and *in vivo* imaging experimental results demonstrate that the permissible source region and multispectral information can both improve the position accuracy, and the reconstruction efficiency is enhanced largely by the efficient iterative shrinkage thresholding method. Our future work will focus on *in vivo* bioluminescence experiments reflecting physiological process and fast reconstruction algorithms on the whole region. The corresponding results will be reported later.

Acknowledgements This research is supported by the National Basic Research Program of China (973 Program) under Grant No. 2011CB707700, the Knowledge Innovation Project of the Chinese Academy of Sciences under Grant No. KGCX2-YW-907, the National Natural Science Foundation of China under Grant No. 81071205, 81027002, 81101084, 30970778, 81090272, 81000632, 30900334, the Fellowship for Young International Scientists of the Chinese Academy of Sciences under Grant No. 2010Y2GA03, the Chinese Academy of Sciences Visiting Professorship for Senior International Scientists under Grant No. 2010T2G36.

Chenghu Qin received the B.S. degree in machine design, manufacture and automation from Tianjin University, Tianjin, China, in 2003, the M.S. degree in signal and information processing from Tianjin University, Tianjin, China, in 2006, and the Ph.D. degree in computer application technology from the Chinese Academy of Sciences, Beijing, China, in 2009. He is currently an Assistant Researcher with the Intelligent Medical Research Center, Institute of Automation, Chinese Academy of Sciences, Beijing, China. His research interests include optical molecular imaging, multimodality fusion, and medical image processing.

Shouping Zhu received the B.S. degree in biomedical engineering and the M.S. degree in signal and information processing from Xidian University, Xi'an, China, in 2004 and 2007, respectively, and the Ph.D. degree in pattern recognition and intelligent systems from the Chinese Academy of Sciences, Beijing, China, in 2010. He is currently a Lecturer with the Life Sciences Research Center, School of Life Sciences and Technology, Xidian University, Xi'an, China. His research interests include medical image processing, microcomputed tomography (CT) system, and CT reconstruction.

Jinchao Feng received the Ph.D. degree in circuit and system from Beijing University of Technology, Beijing, China, in 2010. He is currently a Lecturer with the College of Electronic Information & Control Engineering, Beijing University of Technology, Beijing, China. His research interests include optical molecular imaging, multimodality fusion, and medical image processing.

Jianghong Zhong received the B.S. degree in biomedical engineering from Xi'an Jiaotong University, Xi'an, China, in 2007, and the M.S. degree in biomedical engineering from Beijing Jiaotong University, Beijing, China, in 2009. He is currently a Member with the Intelligent Medical Research Center, Institute of Automation, Chinese Academy of Sciences, Beijing, China. His research interests include multimodality molecular imaging and Cerenkov luminescence tomography.

Xibo Ma received the B.S. degree in biomedical engineering from Shandong University, Jinan, China, in 2004, and the M.S. degree in pharmaceutical engineering from Beijing University of Chemical Technology, in 2008. She is currently a Member with the Intelligent Medical Research Center, Institute of Automation, Chinese Academy of Sciences, Beijing, China. Her research interests include optical molecular imaging, computed tomography, and the applications of molecular imaging.

Ping Wu received the B.S. degree in electrical engineering from the Central South University, Changsha, China, in 2009. She is currently a Ph.D. candidate with the Intelligent Medical Research Center, Institute of Automation, Chinese Academy of Sciences, Beijing, China. Her research interests include optical molecular imaging, computed tomography, and the applications of molecular imaging.

Jie Tian received the Ph.D. degree (with honors) in artificial intelligence from the Institute of Automation, Chinese Academy of Sciences, Beijing, China, in 1992. From 1995 to 1996, he was a Postdoctoral Fellow with the Medical Image Processing Group, University of Pennsylvania, Philadelphia. He is also with the Life Science Center, Xidian University, Xi'an. Since 1997, he has been a Professor with the Intelligent Medical Research Center, Institute of Automation. His current research interests include medical image process and analysis, pattern recognition. Prof. Tian is the Beijing Chapter Chair of the engineering in Medicine and Biology Society of the IEEE.

References

[1] R. Weissleder, Radiology **212**, 609–614 (1999).
[2] R. Weissleder and U. Mahmood, Radiology **219**, 316–333 (2001).
[3] H. R. Herschman, Science **302**, 605–608 (2003).
[4] T. F. Massoud and S. S. Gambhir, Genes Dev. **17**, 545–580 (2003).
[5] R. Weissleder, Science **312**, 1168–1171 (2006).
[6] J. Tian, J. Bai, X. P. Yan, S. Bao, Y. Li, W. Liang, and X. Yang, IEEE Eng. Med. Biol. Mag. **27**, 48–57 (2008).
[7] J. K. Willmann, N. van Bruggen, L. M. Dinkelborg, and S. S. Gambhir, Nature Rev. Drug Discov. **7**, 591–607 (2008).
[8] R. Weissleder and M. J. Pittet, Nature **452**, 580–589 (2008).
[9] V. Ntziachristos, C. H. Tung, C. Bremer, and R. Weissleder, Nature Med. **8**, 757–760 (2002).
[10] R. Weissleder and V. Ntziachristos, Nature Med. **9**, 123–128 (2003).
[11] V. Ntziachristos, J. Ripoll, L. V. Wang, and R. Weissleder, Nature Biotechnol. **23**, 313–320 (2005).
[12] G. Wang, E. A. Hoffman, G. McLennan, L. V. Wang, M. Suter, and J. F. Meinel, Radiology **229**, 566 (2003).
[13] G. Wang, Y. Li, and M. Jiang, Med. Phys. **31**, 2289–2299 (2004).
[14] X. Gu, Q. Zhang, L. Larcom, and H. Jiang, Opt. Exp. **12**, 3996–4000 (2004).
[15] W. Cong, D. Kumar, Y. Liu, A. Cong, and G. Wang, Proc. SPIE **5535**, 679–686 (2004).
[16] G. Wang, W. Cong, H. Shen, X. Qian, M. Henry, and Y. Wang, Front. Biosci. **13**, 1281–1293 (2008).
[17] W. Cong, G. Wang, D. Kumar, Y. Liu, M. Jiang, L. V. Wang, E. A. Hoffman, G. McLennan, P. B. McCray, J. Zabner, and A. Cong, Opt. Exp. **13**, 6756–6771 (2005).
[18] W. Cong and G. Wang, J. Biomed. Opt. **11**, 020503/1–020503/3 (2006).
[19] W. Han, W. Cong, and G. Wang, Inverse Probl. **22**, 1659–1675 (2006).
[20] Y. Lv, J. Tian, W. Cong, G. Wang, J. Luo, W. Yang, and H. Li, Opt. Exp. **14**, 8211–8223 (2006).
[21] H. Dehghani, S. C. Davis, S. Jiang, B. W. Pogue, K. D. Paulsen, and M. S. Patterson, Opt. Lett. **31**, 365–367 (2006).
[22] W. Cong, K. Durairaj, G. Wang, and L. V. Wang, Med. Phys. **33**, 679–686 (2006).
[23] W. Cong, A. Cong, H. Shen, Y. Liu, and G. Wang, Opt. Lett. **32**, 2837–2839 (2007).
[24] H. Dehghani, S. C. Davis, and B. W. Pogue, Med. Phys. **35**, 4863–4870 (2008).
[25] S. Ahn, A. J. Chaudhari, F. Darvas, C. A. Bouman, and R. M. Leahy, Phys. Med. Biol. **53**, 3921–3942 (2008).
[26] Q. Zhang, L. Yin, Y. Tan, Z. Yuan, and H. Jiang, Opt. Exp. **16**, 1481–1486 (2008).
[27] A. D. Klose, B. J. Beattie, L. Vider, C. Le, V. Ponomarev, R. Blasberg, and H. Dehghani, Med. Phys. **37**, 329–338 (2010).
[28] A. Cong, W. Cong, Y. Lu, P. Santago, A. Chatziioannou, and G. Wang, IEEE Trans. Biomed. Eng. **57**, 2229–2238 (2010).
[29] H. Gao and H. Zhao, Opt. Exp. **18**, 1854–1871 (2010).
[30] C. Qin, S. Zhu, and J. Tian, Curr. Pharm. Biotechnol. **11**, 620–627 (2010).
[31] G. Wang, W. Cong, K. Durairaj, X. Qian, H. Shen, P. Sinn, E. Hoffman, G. McLennan, and M. Henry, Opt. Exp. **14**, 7801–7809 (2006).
[32] J. Liu, Y. Wang, X. Qu, X. Li, X. Ma, R. Han, Z. Hu, X. Chen, D. Sun, R. Zhang, D. Chen, D. Chen, X. Chen, J. Liang, F. Cao, and J. Tian, Opt. Exp. **18**, 13102–13113 (2010).
[33] Y. Lu, H. B. Machado, Q. Bao, D. Stout, H. Herschman, and A. F. Chatziioannou, Mol. Imaging Biol. **13**, 53–58 (2011).
[34] J. Feng, K. Jia, G. Yan, S. Zhu, C. Qin, Y. Lv, and J. Tian, Opt. Exp. **16**, 15640–15654 (2008).
[35] A. J. Chaudhari, F. Darvas, J. R. Bading, R. A. Moats, P. S. Conti, D. J. Smith, S. R. Cherry, and R. M. Leahy, Phys. Med. Biol. **50**, 5421–5441 (2005).
[36] Y. Lv, J. Tian, W. Cong, G. Wang, W. Yang, C. Qin, and M. Xu, Phys. Med. Biol. **52**, 4497–4512 (2007).
[37] V. Y. Soloviev, Appl. Optics **46**, 2778–2784 (2007).
[38] C. Kuo, O. Coquoz, T. L. Troy, H. Xu, and B. W. Rice, J. Biomed. Opt. **12**, 024007/1–024007/12 (2007).
[39] G. Wang, H. Shen, Y. Liu, A. Cong, W. Cong, Y. Wang, and P. Dubey, Opt. Exp. **16**, 1719–1732 (2008).
[40] C. Qin, J. Tian, X. Yang, J. Feng, K. Liu, J. Liu, G. Yan, S. Zhu, and M. Xu, Opt. Exp. **17**, 21925–21934 (2009).
[41] K. Liu, X. Yang, D. Liu, C. Qin, J. Liu, Z. Chang, M. Xu, and J. Tian, J. Opt. Soc. Am. A **27**, 1413–1423 (2010).
[42] A. P. Gibson, J. C. Hebden, and S. R. Arridge, Phys. Med. Biol. **50**, R1–R43 (2005).

[43] G. Wang, H. Shen, W. Cong, S. Zhao, and G. W. Wei, Opt. Exp. **14**, 7852–7871 (2006).
[44] J. M. Bioucas-Dias and M. A. T. Figueiredo, IEEE Trans. Image Process. **16**, 2992–3004 (2007).
[45] A. Beck and M. Teboulle, SIAM J. Imag. Sci. **2**, 183–202 (2009).
[46] C. Qin, J. Tian, X. Yang, K. Liu, G. Yan, J. Feng, Y. Lv, and M. Xu, Opt. Exp. **16**, 20317–20333 (2008).
[47] A. D. Klose and E. W. Larsen, J. Comput. Phys. **220**, 441–470 (2006).
[48] M. F. Modest and J. Yang, J. Quant. Spectrosc. Radiat. Transf. **109**, 1641–1666 (2008).
[49] M. Chu, K. Vishwanath, A. D. Klose, and H. Dehghani, Phys. Med. Biol. **54**, 2493–2509 (2009).
[50] Y. Lu, A. Douraghy, H. B. Machado, D. Stout, J. Tian, H. Herschman, and A. F. Chatziioannou, Phys. Med. Biol. **59**, 6477–6493 (2009).
[51] K. Liu, Y. Lu, J. Tian, C. Qin, X. Yang, S. Zhu, X. Yang, Q. Gao, and D. Han, Opt. Exp. **18**, 20988–21002 (2010).
[52] W. Cong, H. Shen, A. Cong, Y. Wang, and G. Wang, Phys. Rev. E **76**, 051913/1–051913/5 (2007).
[53] S. R. Arridge, M. Schweiger, M. Hiraoka, and D. T. Delpy, Med. Phys. **20**, 299–309 (1993).
[54] M. Schweiger, S. R. Arridge, M. Hiraoka, and D. T. Delpy, Med. Phys. **22**, 1779–1792 (1995).
[55] Y. Lu, X. Zhang, A. Douraghy, D. Stout, J. Tian, T. F. Chan, and A. F. Chatziioannou, Opt. Exp. **17**, 8062–8080 (2009).
[56] I. Bayram and I. W. Selesnick, IEEE Trans. Signal Process. **58**, 1131–1143 (2010).
[57] S. Zhu, J. Tian, G. Yan, C. Qin, and J. Feng, Int. J. Biomed. Imag. **2009**, 960573/1–960573/9 (2009).
[58] G. Yan, J. Tian, S. Zhu, Y. Dai, and C. Qin, J. X-Ray Sci. Technol. **16**, 225–234 (2008).
[59] G. Yan, J. Tian, S. Zhu, C. Qin, Y. Dai, F. Yang, D. Dong, and P. Wu, IEEE Trans. Inf. Technol. Biomed. **14**, 1053–1061 (2010).
[60] J. Tian, J. Xue, Y. Dai, J. Chen, and J. Zheng, IEEE Trans. Inf. Technol. Biomed. **12**, 800–812 (2008).
[61] X. Zhang, J. Tian, K. Deng, Y. Wu, and X. Li, IEEE Trans. Biomed. Eng. **57**, 2622–2626 (2010).
[62] H. Li, J. Tian, F. Zhu, W. Cong, L. V. Wang, E. A. Hoffman, and G. Wang, Acad. Radiol. **11**, 1029–1038 (2004).
[63] N. Ren, J. Liang, X. Qu, J. Li, B. Lu, and J. Tian, Opt. Exp. **18**, 6811–6823 (2010).
[64] G. Alexandrakis, F. R. Rannou, and A. F. Chatziioannou, Phys. Med. Biol. **50**, 4225–4241 (2005).
[65] S. A. Prahl, M. J. C. van Gemert, and A. J. Welch, Appl. Optics **32**, 559–568 (1993).